UC Berkeley
UC Berkeley Previously Published Works

Title

Adapting the Electron Beam from SEM as a Quantitative Heating Source for Nanoscale Thermal Metrology

Permalink
https://escholarship.org/uc/item/2m40f4pn

Journal
Nano Letters, 20(5)

ISSN
1530-6984

Authors
Yuan, Pengyu
Wu, Jason Y
Ogletree, D Frank
et al.

Publication Date
2020-05-13

DOI
10.1021/acs.nanolett.9b04940

Supplemental Material
https://escholarship.org/uc/item/2m40f4pn#supplemental

Peer reviewed

eScholarship.org Powered by the California Digital Library
University of California

Adapting the Electron Beam from SEM as a Quantitative Heating Source for Nanoscale Thermal Metrology

Pengyu Yuan,[‖] Jason Y. Wu,[‖] D. Frank Ogletree, Jeffrey J. Urban, Chris Dames,[*] and Yanbao Ma[*]

ABSTRACT: The electron beam (e-beam) in the scanning electron microscopy (SEM) provides an appealing mobile heating source for thermal metrology with spatial resolution of ~1 nm but the lack of systematic quantification of the e-beam heating power limits such application development. Here, we systemically study e-beam heating in LPCVD silicon nitride (SiN_x) thin-films with thickness ranging from 200 to 500 nm from both experiments and complementary Monte Carlo simulations using the CASINO software. There is good agreement about the thickness-dependent e-beam energy absorption of thin-film between modeling predictions and experiments. Using the absorption results we then demonstrate adapting e-beam as a quantitative heat source by measuring the thickness-dependent thermal conductivity of SiN_x thin-films, with the results validated to within 7% by a separate Joule heating experiment. The results described here will open a new avenue to using SEM e-beams as a mobile heating source for advanced nanoscale thermal metrology development.

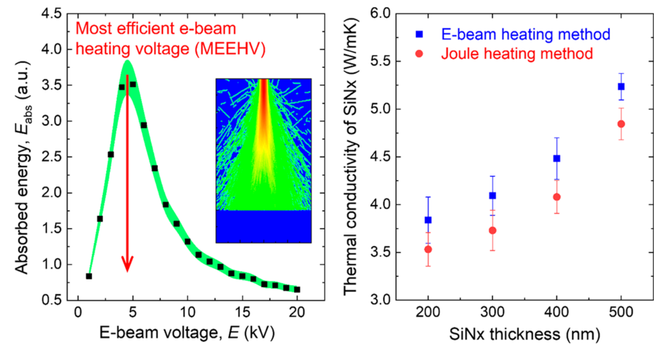

The interaction between the high-kinetic energy electrons from an electron beam (e-beam) and a sample produces a wealth of signals which provide a variety of insights for scanning electron microscopy (SEM), such as analyzing composition, imaging surface morphology, and investigating the crystalline structures. During the electron−substrate interaction, heat is also generated and this makes it possible to apply the e-beam as a high-quality mobile heat source for generating nanoscale thermal hotspots but also for thermal studies in SEM and transmission electron microscopy (TEM).[1−6]

E-beams have several unique characteristics which are appealing for nanoscale thermal metrology. First, an e-beam's potential spatial resolution of ~1 nm is appealing compared to that of alternate techniques for nanoscale thermal measurements, such as the 3ω method, time/frequency-domain thermoreflectance, and Raman/luminescence-based methods, which are generally limited by the microfabrication length scale or optical diffraction limit.[7−9] Similarly, focusing a high-energy e-beam into such a small area results in nanoscale heat sources with extraordinarily high heat fluxes, easily exceeding ~1 MW cm^{-2}. This is valuable for the study of heat dissipation from nanoscale hotspots, which is important for both fundamental understanding and engineering design in micro- and nano-electronics, because nanometer-scale hotspots of up to hundreds of degrees Celsius are believed to influence device performance and reliability.[10] Furthermore, compared to Joule heating by microfabricated heater lines or scanning with a heated atomic force microscope tip,[11,12] the e-beam's dynamically controllable shape and position makes it a more nimble heat source for precise manufacturing and thermal studies.

Understanding e-beam heating is also important for one of the most widespread applications of e-beams, namely imaging in SEM and TEM in which this heating is a critical factor limiting the acquisition of structural or chemical data at high spatial resolution,[13,14] especially for imaging with high e-beam energy in TEM[15,16] and imaging low thermal conductivity materials in SEM.[1,17] Similarly, in e-beam lithography temperature effects on the e-beam resist are a significant contributor to errors in feature size and pattern placement.[18] However, the characterization and quantification of nanoscale e-beam heating is still a topic that has seen little research, especially experimentally.

For imaging, the interactions between the incident e-beam and the target materials are routinely simulated using Monte Carlo (MC) techniques.[19] Especially, the Monte CArlo SImulation of electroN trajectory in sOlids (CASINO)

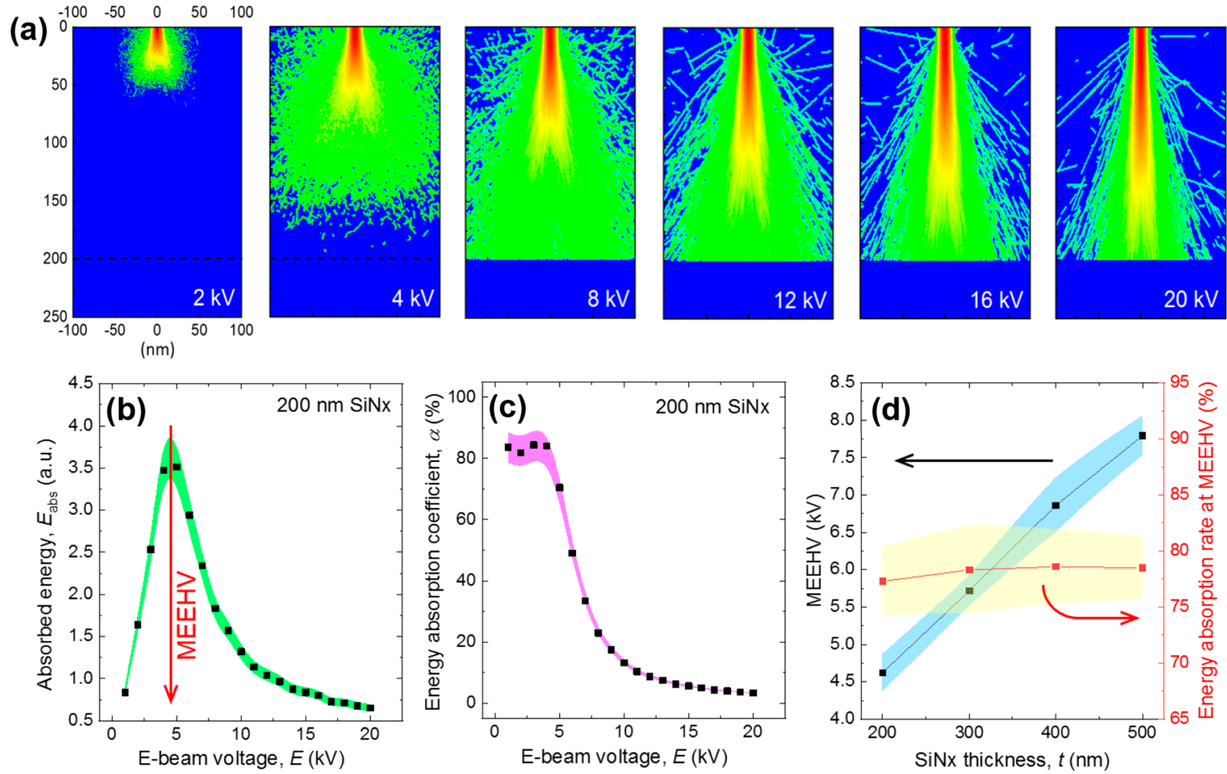

Figure 1. CASINO simulation of electron beam interaction with a 200 nm thick SiN_x thin film (x = 1.33). (a) The distribution of electron energy deposited in the thin film for different primary e-beam energies. The color scale has arbitrary units proportional to absorbed energy density (J/m3 per incident electron). (b) The total absorbed energy in the thin film for various e-beam voltages. The MEEHV value is marked. (c) The energy absorption fraction at different e-beam voltages. (d) The MEEHV (left axis) and energy absorption coefficient at that MEEHV (right axis), as functions of film thickness. The shaded bands in panels b−d represent the effects of varying x from 1.1 to 1.5 in the SiN_x thin film.

software package[20−22] is widely used to simulate the electron−substrate interactions in SEM and has also been applied to develop metrology to estimate thin film thickness based on the intensities of backscattered and secondary electron signals.[23,24] However, the resultant heating phenomena have rarely been considered. One notable example combined MC simulation of the e-beam energy deposition with electron and phonon hydrodynamic transport equations in the substrate, though such calculations have not yet been experimentally validated.[25,26] Indeed, to the best of our knowledge the e-beam energy deposition in thin films as predicted by CASINO has never been experimentally verified.

Early experimental studies of e-beam heating included using thin film thermocouples to measure heating during e-beam lithography[27,28] and the temperature rise of e-beam irradiated freestanding thin films.[29,30] The thin film studies observed a strong and nonmonotonic dependence of the temperature rise on the e-beam voltage,[30] the physics of which was not understood but will be explained in detail below. More recently, e-beam heating in SEM/TEM has been applied for thermal measurements to demonstrate a new microthermometer based on vanadium dioxide nanowire,[1] and to measure the spatially resolved thermal conductance of nanowires[2,3] and two-dimensional materials (graphene,[31] black phosphorus,[32] and MoS_2[33]). However, in all of these previous studies the quantitative power delivered by the e-beam was not used (refs 27−30) or canceled out (refs 1−3) of the final thermal measurement. Therefore, the e-beam has not yet been used as a quantitative heat source for thermal measurement.

In this work, we have studied the e-beam heating of suspended silicon nitride (SiN_x) thin films with thickness ranging from 200 to 500 nm using microfabricated calorimeter devices inside a standard SEM. The results validate the absorption energy profiles calculated by CASINO. Then, for the first time we adapt the e-beam as a quantitative heat source to measure the in-plane thermal conductivity of SiN_x thin films with results in good agreement with independent measurements using a Joule heating method. These results will help develop the application of e-beam as an advanced mobile heating source for future thermal metrologies at the micro- and nanoscale.

■ RESULTS

Theoretical Energy Absorption Study of the Electron Beam in SiN_x Thin Film. As an electron beam interacts with a specimen, the beam undergoes numerous elastic and inelastic scattering events. Besides creating a broad range of signals that can be used for material analysis, here the inelastic interactions are the main focus because they convert energy from the primary e-beam into heat in the specimen. To obtain a statistical understanding of these complex interactions in the specimen, an MC-based electron trajectory simulation can be performed which calculates the paths of numerous incident electrons using random numbers. In this work, we use CASINO v2.5.1.0[20−22] to conduct the MC simulation. Targeting the interaction in SEM, CASINO considers key parameters like the e-beam voltage (the kinetic energy of an incident electron) and the atomic number, thickness, and density of the specimen material. The results are widely

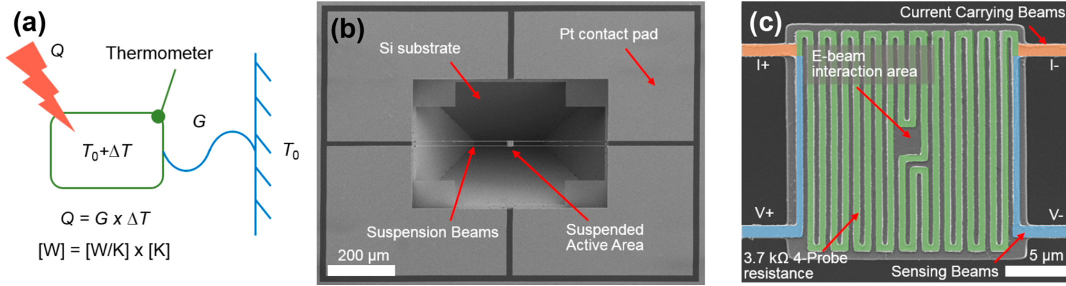

Figure 2. Schematic of the e-beam calorimeter and SEM images of the fabricated devices. (a) The working principle of the calorimeter. The power Q can be determined by measuring the temperature change (ΔT) of the calorimeter using the built-in thermometer and known thermal conductance G. (b) Low-magnification SEM image of the microfabricated SiN_x thin-film based calorimeter. The central suspended area of the device is supported by four 1 μm wide, 300 μm long beams with SiN_x thickness varying from 200 to 500 nm among the various devices. (c) False-color high-magnification image of the central suspended region. The 4-probe PRT is integrated into this island area with the serpentine line (light green) having a resistance of ∼3.7 kΩ between the voltage probes (light blue).

126 accepted for describing the shape and size of the interaction 127 volume, though experimental validation was not previously 128 available regarding the energy deposition.

129 In this work, we choose free-standing SiN_x films as the 130 system for studying e-beam energy absorption because SiN_x is 131 a well-studied structural dielectric used in many micro-132 electronic and MEMS devices.[34,35] To determine the absorbed 133 energy in SiN_x thin films from CASINO simulations, we need 134 to set the specimen information and the microscope 135 conditions. For the specimen, we use three layers, namely a 136 SiN_x thin film sandwiched by the vacuum. The SiN_x chemical 137 composition is specified with the atomic fraction x ranging 138 from 1.1 to 1.5 to match the experimental samples as fabricated 139 by LPCVD and detailed in the following sections. The 140 microscope conditions include the electron beam accelerating 141 voltage, the focused beam size, the number of simulated 142 electron trajectories, and the angle between the specimen 143 normal and the beam direction, and are all set in CASINO to 144 match our experimental conditions. (See Supporting Informa-145 tion Section 1 for more CASINO calculation details.)

146 We first consider CASINO simulations of SiN_x films with 147 thickness t from 200−500 nm and incident e-beam voltages E 148 from 2−20 kV. Note that the e-beam energy will be directly set 149 in the unit of electronvolt (eV) in the CASINO program; 150 however, we will use the accelerating voltage in the unit of volt 151 (V) to quantify the e-beam energy to make direct comparison 152 with following experiment results. As a representative result, f1 153 Figure 1a shows the deposited energy distribution inside a 200 154 nm thick Si_3N_4 (or SiN_x, x = 1.33) thin film for several e-beam 155 voltages. Taking the e-beam voltage of 4 kV, for example, the 156 simulation depicts the cross-section of a bulb-shaped electron− 157 matter interaction volume corresponding to the material of low 158 atomic number (Z = 11.2 for Si_3N_4, averaged based on weight 159 fraction[22]). Materials of higher atomic number (Z > 50) show 160 a more hemispherical shaped interaction volume.[36]

161 For low e-beam voltages when the e-beam penetration depth 162 is smaller than the film thickness, the absorbed energy 163 increases almost linearly with the e-beam voltage as shown 164 in Figure 1b. This corresponds to a nearly constant fraction of 165 each incident electron's energy being absorbed in the film, 166 defined as the electron energy absorption coefficient α, here 167 around 82% as seen in Figure 1c at low energies. We define α 168 such that

169 $$E_{abs} = \alpha E \quad (1)$$

where E is the energy of the incident e-beam and E_{abs} is the 170 corresponding absorbed energy in the film. Even though at low 171 E there is no electron transmission through the sample, the 172 maximum α remains less than 100% because energy is still lost 173 through secondary electrons, backscattered electrons, X-rays, 174 and so forth. 175

Then, upon increasing the e-beam voltage beyond some 176 critical value (∼ 4 kV for 200 nm thick SiN_x) a finite and then 177 increasing fraction of the incident electrons can transmit 178 completely through the film. As a result, α decreases with 179 increasing e-beam voltage. We define the e-beam voltage giving 180 the maximum E_{abs} in Figure 1b as the "most-efficient-e-beam-181 heating-voltage" (MEEHV). For this specimen of 200 nm thick 182 SiN_x, the MEEHV is 4.63 ± 0.35 kV, where the uncertainty 183 range corresponds to varying x from 1.1 to 1.5. When the 184 actual e-beam voltage is below this MEEHV level, the thin film 185 can still absorb most of the incident electrons ($\alpha \approx$ const.), so 186 E_{abs} will increase in direct proportion to E in accordance with 187 eq 1. However, when the e-beam voltage is above this MEEHV 188 electron transmission becomes significant and $\alpha(E)$ falls off 189 more steeply than $1/E$, so that $dE_{abs}/dE < 0$ for E > MEEHV. 190

The thickness dependence of the MEEHV is plotted in 191 Figure 1d. Because thicker films can absorb more electrons at 192 the same incident e-beam energy E, this shifts the MEEHV to 193 larger values for thicker films. The corresponding values of α 194 evaluated at E = MEEHV are shown on the right axis of Figure 195 1d. These calculation results show that the α value at the 196 MEEHV is almost independent of film thickness, even though 197 MEEHV itself is a strong function of thickness. Of course, 198 these quantities also depend on the material, which underlies 199 the shaded uncertainty bands seen in Figure 1d which 200 corresponds to the compositional range $SiN_{1.1}$−$SiN_{1.5}$. 201

From the e-beam matter interaction with its bulb-shaped 202 interaction volume, it is well-known that the location of 203 maximum energy absorption occurs at some finite depth below 204 the specimen surface,[37] which is notably different from optical 205 absorption which is maximal at the surface and exponentially 206 decaying into the specimen (the Beer−Lambert law). The 207 depth of the maximum absorbed e-beam energy is much 208 smaller than the e-beam penetration depth R, which itself is 209 defined as the depth at which 99% of the incident electrons 210 have slowed down to rest. The e-beam penetration depth has 211 been extensively studied both analytically[38] and empirically,[39] 212 and the expression introduced by Kanaya and Okayama is 213 widely used[38] 214

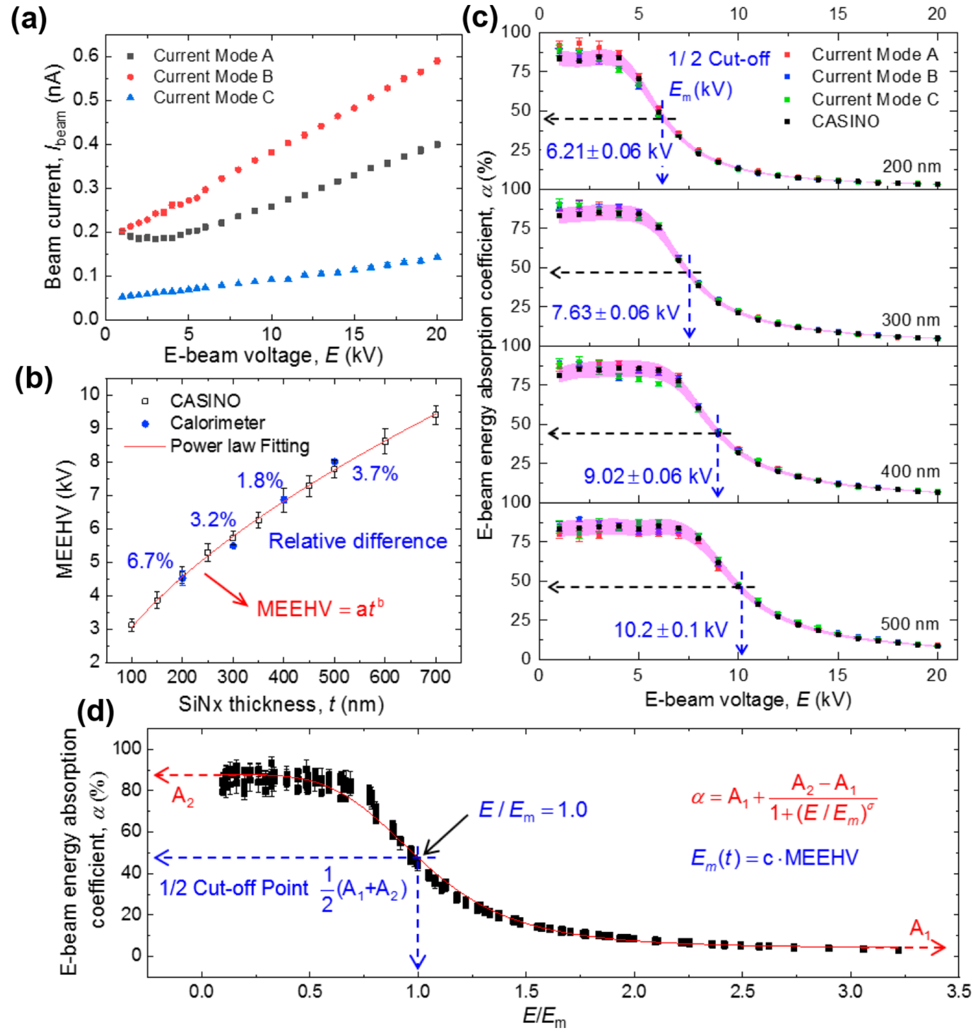

Figure 3. Thickness and current dependence of e-beam absorption. (a) Three current modes used in this work, measured using a Faraday cup. Mode A corresponds to 30 μm aperture size in the normal current setting with a typical error bar of 1.1−3.8%. Mode B corresponds to 30 μm aperture size in the high current setting with a typical error bar of 1.0−3.4%. Mode C corresponds to 20 μm aperture size in the normal current setting with typical error bar of 1.7−4.7%. (b) Comparison of MEEHV values determined theoretically from CASINO and experimentally from calorimeter devices (average of three current modes with error bars showing their standard deviation). The listed percentages give the relative difference between theory and experiment. The power-law fit to the CASINO results yields $a = 0.22 \pm 0.02$ kV and $b = 0.57 \pm 0.02$ with t in nm. (c) The e-beam energy absorption coefficients from CASINO (pink-shaded band represents the effect of varying x from 1.1 to 1.5) compared with experimental results from SiN_x based calorimeter devices of four thickness each with three current modes. The CASINO results for 200 nm thick SiN_x are repeated from Figure 1c. A logistic function is used to fit the results for each thickness with the listed midpoint cutoff energies, E_m. (d) Plot of all 16 sets of data from (c) after rescaling E/E_m (points) and a fit with a universal logistic function (line). $A_1 = 4.07 \pm 0.15$, $A_2 = 88.9 \pm 0.4$, and $c = 0.76 \pm 0.01$.

$$R = \frac{0.0276 \times m_A \times N_A \times E^{5/3}}{(Z^{8/9}) \times \rho} \quad (2)$$

where R is the penetration depth in m, E is the incident e-beam voltage in eV, m_A is the atomic mass in kg, N_A is Avogadro's number, ρ is the density in kg/m^3, and Z is the equivalent atomic number of the specimen. It is also interesting to consider the possibility of nonequilibrium phenomena, which have been studied previously in the context of "aloof" scattering of an e-beam in close proximity to solid matter.[40] That study showed that nonequilibrium phenomena are most prevalent at time scales ($\sim10^{-18}$−10^{-17} s) and length scales ($\sim$1 nm) which are far smaller than those of the present study, suggesting that such nonequilibrium phenomena should only become important for much smaller samples with characteristic lengths below $\sim$10 nm.

Equation 2 shows that the penetration depth increases with the e-beam voltage and thus so does the depth of maximum e-beam energy absorption. When this absorption depth extends beyond the bottom of the thin film, a significant fraction of the incident e-beam power will transmit through the film, and consequently the absorbed energy will decrease. Thus, the energy absorption coefficient α will also decrease even though there is more input energy from the e-beam. These trends are apparent for E larger than $\sim$5 kV in Figure 1b,c.

Experimental Energy Absorption Study of the Electron Beam in SiN_x Thin Films. To measure the absorbed e-beam energy in SiN_x thin films, we microfabricated LPCVD SiN_x-based energy flow calorimeters with built-in platinum resistance thermometers (PRTs) (Figure 2). (see Supporting Information Section 2 for device fabrication details.) The magnitude of the energy flow was quantified by

directly measuring the temperature rise of the calorimeter compared to the surrounding temperature T_0, that is, $\Delta T = T - T_0$. We estimate that there can be an additional temperature rise of up to several degrees Kelvin between the e-beam spot (very center of the island in Figure 2c) and the average temperature of the island which is determined experimentally from the PRT (see Supporting Information Section 6). This additional superposed temperature rise is unimportant for the calorimetry because it is highly localized primarily to within ~100 nm of the e-beam spot and thus does not reach any of the PRT, as well as the fact that the typical ΔT of the calorimeter is much larger, ~50 K.

We first measured the temperature coefficient of resistance (TCR, η) and total thermal conductance (G) (see Supporting Information Sections 4 and 5 for details). It was then mounted in a custom-built SEM holder with electrical feedthroughs for e-beam interaction measurements in a Zeiss Gemini Supra 55VP-SEM. High vacuum conditions (1×10^{-6} Torr) make convection losses negligible. Radiation effects are also negligible, as estimated using a conservative (high) estimate of the emissivity of the SiN_x thin film of about 0.3 (ref 41) which corresponds to an estimated error in the ΔT of the PRT island of less than 1%. When the e-beam is focused on the central open square area, approximately 1 μm × 1 μm as seen in the center of Figure 2c, the absorbed e-beam power will induce a temperature rise ΔT which increases R_{4p} of the PRT.

This SEM has a field emission electron gun with a sub-1 nm focus beam diameter at >15 kV and ~4 nm at 0.1 kV. For e-beam power measurements, we use 10 000 times magnification and a 5.5 mm working distance, and position the focused e-beam at the central SiN_x interaction area is indicated in Figure 2c. Note that the precise location of the e-beam focus position was varied randomly within this ~$(1\ \mu\text{m})^2$ interaction area from trial to trial to average the absorbed energy analysis. The e-beam current I_{beam} depends on the beam voltage as well as the aperture size in the SEM column with larger apertures giving higher current.[42] We studied three different current modes by changing the aperture size (30 and 20 μm) and/or engaging the high-current mode setting of the SEM. The corresponding beam currents are measured separately using a Faraday cup, with results given in Figure 3a. A fixed working distance was used because we found that the beam current was slightly changing at different working distances.

Comparing the Absorbed Energy Determined from Experiment and CASINO. From the calorimeter equation $Q = G\Delta T$ and with ΔT from ΔV_s using eq 2, we measured the absorbed heating power for a given calorimeter device as

$$Q = G \times \frac{\Delta V}{I_s \times R_{4p}(T) \times \eta(T)} \tag{3}$$

For each SiN_x device with known thickness, we measured Q as a function of e-beam voltage and find the MEEHV. In fact, for each thickness we actually determine three MEEHV values by using three different beam current modes. To avoid artifacts from the nonconstant beam current in actual operation (Figure 3a), when determining the experimental MEEHV we use the current-normalized absorbed energy which is rescaled by the reference current at 2 kV

$$\hat{Q}(E) = \frac{Q(E)}{\left[\frac{I_{beam}(E)}{I_{beam}(2\text{kV})}\right]} \tag{4}$$

where $I_{beam}(E)$ is taken from the calibration of Figure 3a. This normalization is justified because one expects $Q(E) \propto I_{beam}(E)$, since each incident electron is an independent event and this was also confirmed by additional experiments. The choice to normalize at the I_{beam} from 2 kV is arbitrary, and any reference I_{beam} could be used without affecting the calculated MEEHV values.

The MEEHV(t) results are shown in Figure 3b with the blue circles representing the experimental values averaged over the three beam currents, which agree closely with the CASINO results. The relative differences between experiments and simulation are also given in the figure, for example, 6.7% for t = 200 nm, 3.2% for 300 nm, and so forth. This agreement not only validates the CASINO model discussed in the first section but also boosts the trust in CASINO to conduct further thermal studies involving electron-matter interaction in SEM. As mentioned in the introduction, previous studies of the e-beam heating of films have been limited to modeling,[23,25,26] and experiments are lacking. Additionally, we extend the CASINO calculation of MEEHV for thicknesses from 100 to 700 nm, and the full range of simulated MHEEV vs thickness is well-fit with a power law as shown by the red line in the figure.

Knowing this, MHEEV(t) relationship has several potential uses. First, in future applications it could be useful for estimating the thickness of suspended thin films. In this work, we have found the MEEHV by using a PRT to measure the temperature rise, which requires additional microfabrication and instrumentation, but in principle the temperature rise could instead be measured directly by SEM thermometry which is less accurate but simpler and noninvasive.[43] Note also that knowledge of G is not needed because it never enters into the calculation of the MEEHV (recall that the MEEHV was found in Figure 1b using arbitrary units on the E-axis). Knowledge of the MEEHV is also helpful for thermal metrologies which use the e-beam as a heater, because operating at the MEEHV gives the peak heating which maximizes the signal-to-noise ratio.[1−3,30] Finally, knowledge of the energy-dependence seen in Figure 1b is also helpful for optimizing e-beam conditions in standard SEM/TEM imaging of suspended samples. Normally low-E imaging can result in notable charging effects because low-energy electrons will be easily left on the surface, so it is intuitive to increase the beam voltage to reduce the charging effect, but this increased electron beam voltage raises obvious concerns about damaging the sample through overheating. However, Figure 1b shows that choosing $E \gg$ MEEHV may be most favorable of all, because it reduces charging as well as reducing the heat deposited in the sample.

When evaluating the e-beam energy absorption coefficients, α_{CASINO} is statistically determined by tracing all the simulated primary electrons. The experimental values from the calorimeter were calculated as $\alpha = Q/(I_{beam}E)$ and compared with the CASINO results in Figure 3a. We determined $\alpha(E, t)$ from the calorimeter for the three different current modes, and in all cases the results are in good agreement with the CASINO simulations as shown in Figure 3c. This detailed experimental and theoretical understanding of $\alpha(E, t)$ provides the foundation to apply the e-beam as a quantitative heating source for nanoscale thermal metrologies, as demonstrated in the next section for SiN_x thin films.

To simplify the energy absorption coefficient of SiN_x thin films at different e-beam voltage, for each film thickness in

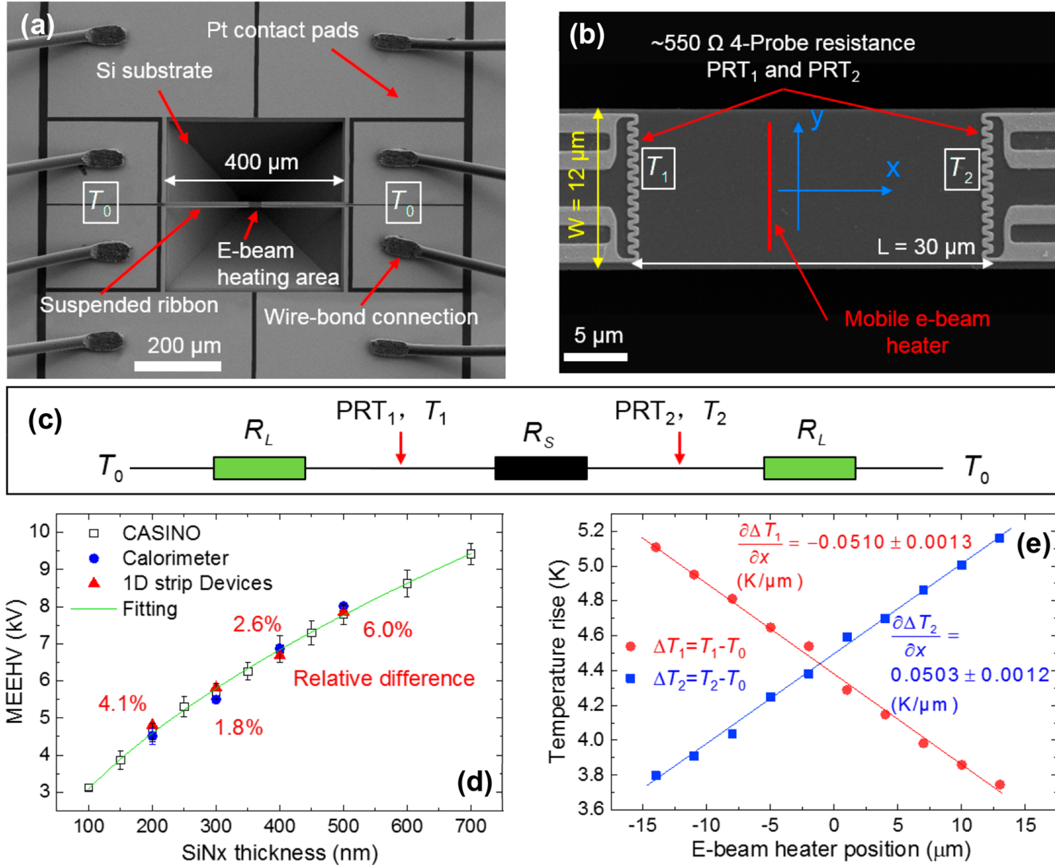

Figure 4. The 1D ribbon device structure for SiN_x thermal conductivity measurement using e-beam heating. (a) Low-magnification SEM image of the microfabricated device. The suspended portion is 430 μm long (considering undercut) and 12 μm wide with SiN_x thickness ranging from 200 to 500 nm. (b) High-magnification image of the central suspended region which is also the e-beam heating area. (c) The thermal circuit of the 1D SiN_x ribbon device. R_s represents the thermal resistance between the two PRTs. (d) The thickness of these device is confirmed by their MEEHVs (red triangles), which lie very close to previous results repeated from Figure 3b. (e) Temperature rise at the two PRTs as a function of e-beam heater location x, for the 200 nm thick device.

364 Figure 3c we empirically fit the e-beam absorption results with
365 a logistic function

$$\alpha(E) = A_1 + \frac{A_2 - A_1}{1 + \left(\frac{E}{E_m}\right)^{\sigma}} \tag{5}$$
366

367 where A_2 is the low-E plateau absorptivity, E_m is a characteristic
368 midpoint energy at which $\alpha(E) = (A_1 + A_2)/2$, and σ
369 parametrizes the sharpness of the transition. The fit values of
370 E_m are given in the figure and closely follow a power law $E_m =$
371 at^b, where the thickness t is in nm and E_m is in kV. This power-
372 law exponent is similar to the value 5/3 in the Kanaya-
373 Okayama range of eq 2, and we also find that $E_m(t) = (0.79 \pm$
374 $0.01) \times$ MEEHV(t) at least over this range of thicknesses.
375 Such similarity is not surprising considering that they all
376 originate from the same physical mechanism of the e-beam
377 penetration depth reaching and then exceeding the film
378 thickness.

379 For each plot in Figure 3c, there is relatively large data
380 variation for $E < E_m$ and better consistency for $E > E_m$. The
381 absorption coefficient α shown here is an average over various
382 e-beam spot locations in the central ~1 μm interaction area in
383 Figure 2c. For lower e-beam voltages, we found that the
384 charging effects varied significantly among these spot locations,
385 causing the notable variation. This effect was more limited
386 when higher e-beam voltage ($E > E_m$) was applied.

Finally, in Figure 3d we collapse all of the results from 387
Figure 3c into a single universal logistic function, 388
$\alpha(E, t) = A_1 + \frac{(A_2 - A_1)}{1 + \left[\frac{E}{E_m(t)}\right]^{\sigma}}$, where $E_m(t) = ct^b$ and the fit
values for a, b, c, A_1, A_2, and σ are given in the figure for SiN_x 389
and are independent of E and t. The points shown in this plot 390
comprise all 16 sets of data from Figure 3c, both experimental 391
and from CASINO, with the x-axis rescaled by dividing E by 392
each thickness' corresponding $E_m(t)$. The generally excellent 393
collapse of data seen in Figure 3d after this rescaling confirms 394
that for each thickness there is fundamentally only one 395
characteristic energy scale, whether it is discussed as 396
MEEHV(t), $E_m(t)$, or the inversion of eq 2 after equating R 397
and t, namely $E_{KO}(t) = \left(\frac{\rho z^{8/9} t}{0.0276 m_A N_A}\right)^{3/5}$.
398

**Demonstration of E-Beam as a Quantitative Heating 399
Source for Thermal Metrology: Measuring the Thermal 400
Conductivity of SiN_x Thin Films.** Building on the above 401
calorimeter and CASINO study of the e-beam energy 402
absorption in SiN_x thin films, we are now able to use the e- 403
beam for quantitative thermal analysis. In this section, we will 404
demonstrate using the e-beam heater to determine the in-plane 405
thermal conductivity of LPCVD SiN_x thin films, and the results 406
are confirmed by independent measurements using a Joule- 407
heating method. As mentioned above, amorphous silicon 408

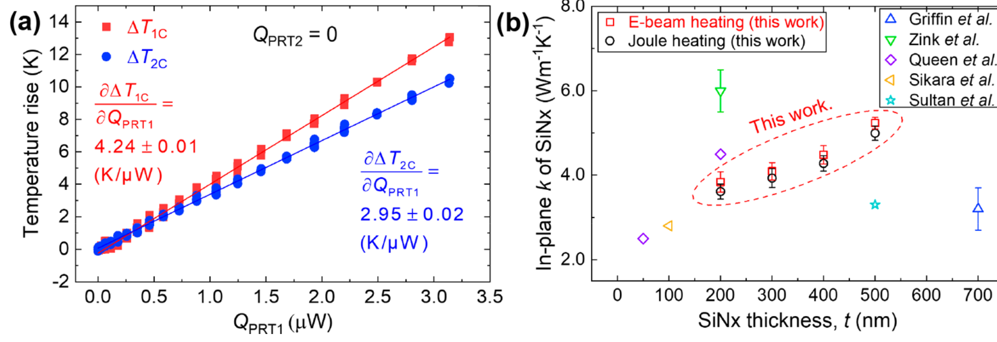

Figure 5. Joule heating approach to measure k of the 1D ribbon devices. (a) Results for the 200 nm thick device: temperature rises of the two PRTs in response to Joule heating by PRT_1. (b) Comparison of SiN_x thermal conductivity at room temperature as determined by the e-beam heating and Joule heating methods. Literature results are from refs 4−6, 50, 61, and 62.

nitride is commonly used in many microelectronic and MEMS devices, including suspended structures.[34,35,44] As such, knowledge of the in-plane thermal conductivity of SiN_x films is important as microfabricated heaters and thermal sensors are thermally isolated from the environment using these suspended structures. Furthermore, the thermal conductivity of SiN_x films can depend on stoichiometry, growth conditions, and film thickness, so it is generally not accurate to simply take a reference value from the literature.

As shown in Figure 4a, we prepared free-standing SiN_x ribbon devices using the same processing steps as the calorimeter. The suspended area is 430 μm long and 12 μm wide which justifies approximating the heat flows as 1D along the x-direction of the SiN_x ribbon. The SiN_x ribbon thickness of different devices ranges from 200 to 500 nm, and is shown in Figure 4d. Measurements of the MEEHV verrsus thickness for these suspended ribbon devices shows nearly identical response as the previous measurements on calorimeter devices and CASINO simulations. At the central area of the ribbon (Figure 4b), there are two 4-probe PRTs which can serve as both heater and thermometer, separated by a distance L = 30 μm. Each PRT's 4-probe electrical resistance is around 550 Ω, and their TCRs are calibrated to measure the local temperature rise (see Supporting Information Section 4).

The basic principle of the thermal conductivity measurement is depicted in Figure 4b,c. The e-beam was used as a line heat source at a location x, causing steady-state 1D heat flow (along $\pm x$ directions) in the SiN_x ribbon to the Si substrate which acts as a heat sink at T_0. Two PRTs measured the resulting temperatures T_1 and T_2 as functions of the e-beam location x, which as detailed next can be used to determine k, the in-plane thermal conductivity of the SiN_x thin film.

In developing the detailed thermal analysis model, convection and radiation losses were both estimated to be negligible. To experimentally justify a 1D analysis along the x-direction, we first used local e-beam heating to investigate possible 2D effects. With the e-beam in spot mode at a fixed x coordinate near $x = 0$, we moved the e-beam along y and found that the temperature rises at each of the two PRTs were independent of the e-beam spot's y location to within 2%. This variation is mainly random but higher whenever the e-beam focused on some rough areas (appearing as whiter dots in the SEM image) which affects the interaction between e-beam and the thin film. To average out these variations and even better approximate 1D heat conduction, for all subsequent measurements we control the e-beam to approximate a line heating source, by rapidly scanning the focused e-beam along the y-direction between +5 μm and −5 μm. This scanning is realized by a Python-based software platform (ScopeFoundry)[45] instead of using the default Smart SEM software from Zeiss. The scanning rate is set as 500 kHz.

In the thermal model, define R_L as the thermal resistance (K/W) of each of the ~200 μm long suspended ribbon sections between the heat sink and the PRTs. Because of the symmetry of the microfabrication, the two R_Ls are nominally identical, namely the left R_L between T_0 and T_1 and the right R_L between T_0 and T_2. Note that R_L includes the parallel conduction pathways of the SiN_x thin film and the Pt lines on top. Similarly, the thermal resistance of the SiN_x between the two PRTs is

$$R_S = \frac{L}{A \times k} \tag{6}$$

where $A = wt$ is the cross-sectional area of the ribbon, w = 12 μm is the ribbon width, L = 30 μm is the distance between two PRTs, and k is the in-plane thermal conductivity of the SiN_x thin film.

With the e-beam heating line localized a station x as indicated in Figure 4b, two equivalent expressions for the heat flow to the left are

$$Q_1 = \frac{\Delta T_1}{R_L} = \frac{\Delta T_i(x) - \Delta T_1(x)}{R_i(x)} \tag{7}$$

where $\Delta T_1 = T_1 - T_0$ is temperature rise measured by left PRT, $\Delta T_i(x) = T_i(x) - T_0$ represents the temperature rise at the e-beam heating position x which cannot be directly measured in this experiment, and $R_i(x) = (L/2 + x)/(kA)$ is the thermal resistance between the e-beam heating position x and the left PRT. Likewise, considering the heat flow going to the right, we have

$$Q_2 = \frac{\Delta T_2}{R_L} = \frac{\Delta T_i(x) - \Delta T_2(x)}{R_s - R_i(x)} \tag{8}$$

From the overall energy balance, the total absorbed e-beam energy (Q) is finally conducted to the heat sink through both ends ($Q = Q_1 + Q_2$), so we have

$$Q = \frac{\Delta T_1 + \Delta T_2}{R_L} \tag{9}$$

Then we eliminate ΔT_i from eqs 7 and 8 to have $\Delta T_1 R_i - \Delta T_2(R_S - R_i) = (\Delta T_2 - \Delta T_1)R_L$. Differentiating this equation with respect to x and using eq 9 to represent R_L, we can express the thermal conductivity k as

$$k = Q \times \frac{(\Delta T_1 + \Delta T_2) - \frac{\partial \Delta T_2}{\partial x} \times L}{(\Delta T_1 + \Delta T_2) \times A \times \frac{\partial(\Delta T_2 - \Delta T_1)}{\partial x}} \quad (10)$$

where eq 9 also shows that the sum $(\Delta T_1 + \Delta T_2)$ is independent of x, which further implies $\partial\Delta T_1/\partial x = -\partial\Delta T_2/\partial x$. In the experiment, we determine $\partial\Delta T_1/\partial x$ and $\partial\Delta T_2/\partial x$ by placing the e-beam heating line at different x-positions. Here, we use Current Mode A and operate at each thickness' corresponding MEEHV value to maximize the signal-to-noise ratio. Typical results for the 200 nm thick ribbon device are shown in Figure 4e, which confirms the expected symmetries of $\partial\Delta T_1/\partial x = -\partial\Delta T_2/\partial x$ to within 1.5%. For this device, k is found from eq 10 to be 3.84 ± 0.24 W m^{-1} K^{-1}.

The results for thickness-dependent thermal conductivity using this new e-beam based method are plotted as empty squares in Figure 5b, which shows that k increases from 3.84 to 5.23 W m^{-1} K^{-1} as t increases from 200 to 500 nm. We have shown that with error bars with 7%, the largest sources of error include fitting results of $\partial\Delta T_1/\partial x$ and $\partial\Delta T_2/\partial x$, and the absorbed e-beam energy evaluation from the calorimeter. The general trend of increasing $k(t)$ is very well established for thin films due to boundary scattering of long mean-free-path phonons at the film surfaces which reduces k for small t, as is frequently modeled using the Fuchs−Sondheimer solution of the Boltzmann transport equation.[46−48] For the amorphous silicon nitride studied in this work, its thermal conductivity has been previously reported to contain a significant contribution from long-mean-free-path propagons as compared to non-propagating modes,[49] so thin-film size effects play a role in thermal conduction. Figure 5b also shows that these measured k values are comparable to other literature reports for suspended LPCVD SiN_x with a thickness below 800 nm. Fifty and 200 nm thick suspended LPCVD SiN_x membranes were ~2.5 and ~4.5 W m^{-1} K^{-1} respectively.[5] The ~2.8 W m^{-1} K^{-1} was reported for a 100 nm thick LPCVD SiN_x film,[50] ~3.3 W m^{-1} K^{-1} for 500 nm thick SiN_x bridge,[6] and so forth.

To validate the $k(t)$ measurements from the e-beam heating method, we also implemented a Joule heating method to independently measure k in the same structures. In this technique, we used PRT_1 as a heater and both PRTs as temperature sensors. The analysis would be simplest if the Joule heating were localized purely at PRT_1, but the two DC current-carrying leads also contribute Joule heat which must be taken into account. Therefore, we conducted two sets of experiments (designated Case A and Case B in the Supporting Information Section 7) and used a superposition argument to determine the equivalent response to localized Joule heating at only the left PRT (Q_{PRT1}), called Case C. Focusing on Case C, just as in the e-beam heating method the localized Joule heating from PRT_1 will flow to both to left and right heat sinks. Considering the heat flow to the left (Q_{PRT1_1}), we have

$$Q_{PRT1_1} = \frac{\Delta T_{1C}}{R_L} \quad (11)$$

where $\Delta T_{1C} = T_{1C} - T_0$ is the temperature rise of heating PRT_1 for case C. Similarly, the heat flow to the right is

$$Q_{PRT1_2} = \frac{\Delta T_{1C} - \Delta T_{2C}}{R_S} \quad (12)$$

also

$$Q_{PRT1_2} = \frac{\Delta T_{2C}}{R_L} \quad (13)$$

where ΔT_{2C} is the temperature rise of the sensing PRT_2. Also from the overall energy balance, the Joule heating at the left PRT (Q_{PRT1}) is finally conducted to the heat sink through both ends, $Q_{PRT1} = Q_{PRT1_1} + Q_{PRT1_2}$, so we have

$$Q_{PRT1} = \frac{\Delta T_{1C} + \Delta T_{2C}}{R_L} \quad (14)$$

As derived in detail in the Supporting Information Section 7, the thermal conductivity of the SiN_x thin film can be determined by

$$k = \frac{L}{A \times \left(\frac{\partial T_{1C}/\partial Q_{PRT1}}{\partial T_{2C}/\partial Q_{PRT1}} + 1\right) \times \left(\frac{\partial T_{1C}}{\partial Q_{PRT1}} - \frac{\partial T_{2C}}{\partial Q_{PRT1}}\right)} \quad (15)$$

An example of the raw data for this measurement is given in Figure 5a for a 200 nm thick SiN_x thin film. Using eq 15, we find $k = 3.61 \pm 0.18$ W m^{-1} K^{-1} which is only 6.3% smaller than the k-value determined from the e-beam heating method. These measurements for all four thicknesses are compared in Figure 5b, with mutual agreement between e-beam and Joule heating measurements always better than 7%. The error bars for the Joule heating results come from the uncertainty in TCR and electrical resistance and the variation between k-values as determined using PRT1 (e.g., as shown in Figure 5a) and PRT2 (not shown in Figure 5; see Supporting Information Section 7).

Comparing heating by the e-beam versus Joule heating of a PRT, the e-beam heating approach offers several advantages. First, although the e-beam based k-measurements in this study required additional microfabrication to create the PRT, in principle the temperature could instead be measured directly using the SEM[43,51] or TEM[52−56] itself. This will greatly simplify the microfabrication and make the e-beam heating and sensing at arbitrary locations and with various shapes. Second, an e-beamline heater can be narrower than a lithographically defined PRT, better concentrating the heat source and simplifying analysis. Similarly, the e-beam better approximates a sheet source in the yz plane, whereas a PRT heater is a surface source whose heat must diffuse further down in the z-direction before it can flow purely along $\pm x$. On the other hand, the Joule heating delivered by a PRT can be measured more accurately, and has the potential to deliver much larger heating powers and thus greater temperature differences than the e-beam. This last point can be a serious restriction and means the e-beam heating approach is most appropriate for samples of relatively low thermal conductance G, that is, long, thin, and low-k.

The thermal conductivity measurement technique demonstrated here on silicon nitride can in principle also be adapted to study thin films of other materials, such as polysilicon, silicon carbide, and metals. For crystalline materials, it is intriguing to recognize the possibility of directly measuring subcontinuum heat conduction phenomena, since the characteristic dimensions of the heater spot size as well as heater placement accuracy (both ~10 nm) are much smaller than the intrinsic MFPs (mean free paths) in crystalline materials, which are typically in the range from ~100 nm -10 μm around room temperature.[57−59] For such measurements, a modified version of the device shown in Figure 4 could be

microfabricated with the PRTs as narrow straight lines of width 100 nm or less rather than the 1 μm effective widths of the serpentine PRTs used here. Then, by placing the e-beam heater line even closer to a PRT, at small heater−thermometer separations the effective temperature rise seen at the PRT should deviate from the Fourier law prediction due to ballistic phonon effects, although the precise nature of this deviation would have to be calculated using a more sophisticated sub-continuum framework like the Boltzmann transport equation. Another interesting direction for future work would be to rotate the orientation of the e-beam heater line, thereby interrogating anisotropic heat conduction along different directions; this would be the e-beam and nanoscale analog of a recently demonstrated elliptical Gaussian beam laser technique.[60]

We also note a limitation when extending this new thermal metrology to other materials. Although the results from the first part of this study show that the e-beam energy deposition as calculated by CASINO is reliable for silicon and nitrogen, and we see no reason to doubt CASINO, nevertheless if applying this new thermal metrology to other materials additional measurements of the energy absorption are recommended before fully relying on such simulations.

■ DISCUSSION

We demonstrate how an e-beam can be used as a quantitative mobile heating source and apply it to perform thermal measurements at the nanoscale. Experiments using microfabricated calorimeter SiN_x devices of varying film thickness and e-beam energy validate the electron energy deposition predictions of the widely used Monte Carlo simulation program CASINO. These energy absorption results provide a foundation to exploit the e-beam as a quantitative mobile heating source for nanoscale thermal metrology. We demonstrate this capability by measuring the in-plane thermal conductivity of SiN_x thin films of varying thickness with results in good agreement with independent measurements using a Joule heating method. This study shows how the electron beam in an SEM has the potential to develop into a practical tool for noncontact thermal measurements at the nanoscale.

■ ASSOCIATED CONTENT

Supporting Information

The Supporting Information is available free of charge at https://pubs.acs.org/doi/10.1021/acs.nanolett.9b04940.

CASINO calculation, device fabrication, Joule heating method details (PDF)

■ AUTHOR INFORMATION

Corresponding Authors

Chris Dames − *Department of Mechanical Engineering, University of California, Berkeley, California 94720, United States*; Email: cdames@berkeley.edu

Yanbao Ma − *Department of Mechanical Engineering, University of California, Merced, California 95343, United States*; orcid.org/0000-0001-9721-3333; Email: yma5@ucmerced.edu

Authors

Pengyu Yuan − *Department of Mechanical Engineering and Department of Mechanical Engineering, University of California, Berkeley, California 94720, United States; The Molecular Foundry, Lawrence Berkeley National Laboratory, Berkeley, California 94720, United States*

Jason Y. Wu − *Department of Mechanical Engineering, University of California, Berkeley, California 94720, United States*

D. Frank Ogletree − *The Molecular Foundry, Lawrence Berkeley National Laboratory, Berkeley, California 94720, United States*

Jeffrey J. Urban − *The Molecular Foundry, Lawrence Berkeley National Laboratory, Berkeley, California 94720, United States*; orcid.org/0000-0002-6520-830X

Author Contributions

‖P.Y and J.Y.W. contributed equally to this work.

Author Contributions

P.Y. performed the CASINO simulation and the experiments of energy absorption, e-beam heating, and Joule heating thermal conductivity measurement with the help of J.Y.W. and D.F.O. Also, J.Y.W. and P.Y. designed and fabricated the calorimeter and 1D ribbon devices. P.Y., C.D., Y.M, and J.J.U. wrote the manuscript. All authors discussed the results and commented on the manuscript.

Notes

The authors declare no competing financial interest.

■ ACKNOWLEDGMENTS

The authors gratefully acknowledge the funding from the Air Force Office of Scientific Research under Contract No. FA9550-18-1-0086 and National Science Foundation (Award Number: 1637370), and support from Molecular Foundry under proposals No. 5842 and No. 6166. This work was partially performed at the Molecular Foundry, Lawrence Berkeley National Laboratory and was supported by the Office of Science, Office of Basic Energy Sciences, Scientific User Facilities Division, of the U.S. Department of Energy under Contract No. DE-AC02-05CH11231. The authors would like to thank Ed Wong for technical assistance.

■ REFERENCES

(1) Guo, H.; Khan, M.; Cheng, C.; Fan, W.; Dames, C.; Wu, J.; Minor, A. Vanadium dioxide nanowire-based microthermometer for quantitative evaluation of electron beam heating. *Nat. Commun.* **2014**, *5*, 4986.

(2) Lee, S.-Y.; Lee, W.-Y.; Thong, J. T.; Kim, G.-S.; Lee, S.-K. Lateral heat flow distribution and defect-dependent thermal resistance in an individual silicon nanowire. *Nanotechnology* **2016**, *27*, 115402.

(3) Liu, D.; Xie, R.; Yang, N.; Li, B.; Thong, J. T. Profiling nanowire thermal resistance with a spatial resolution of nanometers. *Nano Lett.* **2014**, *14*, 806−812.

(4) Zink, B.; Hellman, F. Specific heat and thermal conductivity of low-stress amorphous Si−N membranes. *Solid State Commun.* **2004**, *129*, 199−204.

(5) Queen, D.; Hellman, F. Thin film nanocalorimeter for heat capacity measurements of 30 nm films. *Rev. Sci. Instrum.* **2009**, *80*, No. 063901.

(6) Sultan, R.; Avery, A.; Stiehl, G.; Zink, B. Thermal conductivity of micromachined low-stress silicon-nitride beams from 77 to 325 K. *J. Appl. Phys.* **2009**, *105*, No. 043501.

(7) Lee, S.-M.; Cahill, D. G. Heat transport in thin dielectric films. *J. Appl. Phys.* **1997**, *81*, 2590−2595.

(8) Paddock, C. A.; Eesley, G. L. Transient thermoreflectance from thin metal films. *J. Appl. Phys.* **1986**, *60*, 285−290.

(9) Schmidt, A. J.; Cheaito, R.; Chiesa, M. A frequency-domain thermoreflectance method for the characterization of thermal properties. *Rev. Sci. Instrum.* **2009**, *80*, No. 094901.
(10) Pop, E. Energy dissipation and transport in nanoscale devices. *Nano Res.* **2010**, *3*, 147−169.
(11) Grosse, K. L.; Bae, M.-H.; Lian, F.; Pop, E.; King, W. P. Nanoscale Joule heating, Peltier cooling and current crowding at graphene−metal contacts. *Nat. Nanotechnol.* **2011**, *6*, 287.
(12) Chapuis, P.-O.; Greffet, J.-J.; Joulain, K.; Volz, S. Heat transfer between a nano-tip and a surface. *Nanotechnology* **2006**, *17*, 2978.
(13) Egerton, R.; Li, P.; Malac, M. Radiation damage in the TEM and SEM. *Micron* **2004**, *35*, 399−409.
(14) Groves, T. Theory of beam-induced substrate heating. *J. Vac. Sci. Technol., B: Microelectron. Process. Phenom.* **1996**, *14*, 3839−3844.
(15) Leijten, Z. J.; Keizer, A. D.; de With, G.; Friedrich, H. Quantitative analysis of electron beam damage in organic thin films. *J. Phys. Chem. C* **2017**, *121*, 10552−10561.
(16) Liu, M.; Xu, L.; Lin, X. Heating effect of electron beam bombardment. *Scanning* **1994**, *16*, 1−5.
(17) Almasi, G.; Blair, J.; Ogilvie, R.; Schwartz, R. A Heat-Flow Problem in Electron-Beam Microprobe Analysis. *J. Appl. Phys.* **1965**, *36*, 1848−1854.
(18) Yasuda, M.; Kawata, H.; Murata, K.; Hashimoto, K.; Hirai, Y.; Nomura, N. Resist heating effect in electron beam lithography. *J. Vac. Sci. Technol., B: Microelectron. Process. Phenom.* **1994**, *12*, 1362−1366.
(19) Joy, D. C. *Monte Carlo modeling for electron microscopy and microanalysis*; Oxford University Press, 1995; Vol. *9*.
(20) Hovington, P.; Drouin, D.; Gauvin, R. CASINO: A new Monte Carlo code in C language for electron beam interaction—Part I: Description of the program. *Scanning* **1997**, *19*, 1−14.
(21) Drouin, D.; Hovington, P.; Gauvin, R. CASINO: A new monte carlo code in C language for electron beam interactions—part II: Tabulated values of the mott cross section. *Scanning* **1997**, *19*, 20−28.
(22) Hovington, P.; Drouin, D.; Gauvin, R.; Joy, D. C.; Evans, N. CASINO: A new Monte Carlo code in C language for electron beam interactions—part III: Stopping power at low energies. *Scanning* **1997**, *19*, 29−35.
(23) Movla, H.; Babazadeh, M. Simulation analysis of the aluminum thin film thickness measurement by using low energy electron beam. *Optik* **2014**, *125*, 71−74.
(24) Tian, J.; Wu, J.; Chiu, Y.-L. Monte Carlo simulation and theoretical calculation of SEM image intensity and its application in thickness measurement. *Ultramicroscopy* **2018**, *187*, 13−19.
(25) Wong, B. T.; Mengüç, M. P. Analysis of electrical and thermal responses of n-doped silicon to an impinging electron beam and joule heating. *Int. J. Heat Mass Transfer* **2009**, *52*, 2632−2645.
(26) Wong, B. T.; Pinar Menguc, M. A unified Monte Carlo treatment of the transport of electromagnetic energy, electrons, and phonons in absorbing and scattering media. *J. Quant. Spectrosc. Radiat. Transfer* **2010**, *111*, 399−419.
(27) Chu, D.; Bilir, D. T.; Pease, R. F. W.; Goodson, K. E. Submicron thermocouple measurements of electron-beam resist heating. *J. Vac. Sci. Technol., B: Microelectron. Process. Phenom.* **2002**, *20*, 3044−3046.
(28) Chu, D.; Wong, W.-K.; Goodson, K. E.; Pease, R. F. W. Transient temperature measurements of resist heating using nano-thermocouples. *J. Vac. Sci. Technol., B: Microelectron. Process. Phenom.* **2003**, *21*, 2985−2989.
(29) Wang, Z.; Gui, L.; Han, D.; Xu, Z.; Han, L.; Xu, S. Measurement and Evaluation of Local Surface Temperature Induced by Irradiation of Nanoscaled or Microscaled Electron Beams. *Nanoscale Res. Lett.* **2019**, *14*, 31.
(30) Wang, Z.; Yang, F.; Han, D.; Li, G.; Xu, J.; Xu, S. Alternative method to fabricate microdevices on a freestanding Si3N4 window. *J. Vac. Sci. Technol., B: Nanotechnol. Microelectron.: Mater., Process., Meas., Phenom.* **2017**, *35*, No. 041601.
(31) Wang, Z.; Xie, R.; Bui, C. T.; Liu, D.; Ni, X.; Li, B.; Thong, J. T. Thermal transport in suspended and supported few-layer graphene. *Nano Lett.* **2011**, *11*, 113−118.
(32) Zhao, Y.; Zhang, G.; Nai, M. H.; Ding, G.; Li, D.; Liu, Y.; Hippalgaonkar, K.; Lim, C. T.; Chi, D.; Li, B.; Wu, J.; Thong, J. T. L. Probing the Physical Origin of Anisotropic Thermal Transport in Black Phosphorus Nanoribbons. *Adv. Mater.* **2018**, *30*, 1804928.
(33) Aiyiti, A.; Bai, X.; Wu, J.; Xu, X.; Li, B. Measuring the thermal conductivity and interfacial thermal resistance of suspended MoS2 using electron beam self-heating technique. *Science Bulletin* **2018**, *63*, 452−458.
(34) Prodanović, V.; Chan, H.; Graaf, H.; Sarro, P. Ultra-thin alumina and silicon nitride MEMS fabricated membranes for the electron multiplication. *Nanotechnology* **2018**, *29*, 155703.
(35) Bagolini, A.; Savoia, A. S.; Picciotto, A.; Boscardin, M.; Bellutti, P.; Lamberti, N.; Caliano, G. PECVD low stress silicon nitride analysis and optimization for the fabrication of CMUT devices. *J. Micromech. Microeng.* **2015**, *25*, No. 015012.
(36) Niedrig, H. Electron backscattering from thin films. *J. Appl. Phys.* **1982**, *53*, R15−R49.
(37) Neubert, G.; Rogaschewski, S. Measurements of the back-scattering and absorption of 15−60 keV electrons for transparent solid films at various angles of incidence. *J. Phys. D: Appl. Phys.* **1984**, *17*, 2439.
(38) Kanaya, K. a.; Okayama, S. Penetration and energy-loss theory of electrons in solid targets. *J. Phys. D: Appl. Phys.* **1972**, *5*, 43.
(39) Fitting, H. J. Transmission, energy distribution, and SE excitation of fast electrons in thin solid films. *physica status solidi (a)* **1974**, *26*, 525−535.
(40) Lagos, M. J.; Reyes-Coronado, A.; Konečná, A.; Echenique, P. M.; Aizpurua, J.; Batson, P. E. Attosecond and femtosecond forces exerted on gold nanoparticles induced by swift electrons. *Phys. Rev. B: Condens. Matter Mater. Phys.* **2016**, *93*, 205440.
(41) Yuehui, Y.; Xianghuai, L.; Ziwei, F.; Shichang, Z. Optical properties and microstructure of silicon nitride film synthesized by ion beam enhanced deposition. *Appl. Surf. Sci.* **1989**, *40*, 145−150.
(42) Lim, S.-J.; Lee, C.-H. In *Analysis of probe current in scanning electron microscopy*; 2008 International Conference on Control, Automation and Systems, 2008; IEEE: 2008; pp 1200−1203.
(43) Khan, M.; Lubner, S.; Ogletree, D.; Dames, C. Temperature dependence of secondary electron emission: A new route to nanoscale temperature measurement using scanning electron microscopy. *J. Appl. Phys.* **2018**, *124*, 195104.
(44) Dong, J.; Du, P.; Zhang, X. Characterization of the Young's modulus and residual stresses for a sputtered silicon oxynitride film using micro-structures. *Thin Solid Films* **2013**, *545*, 414−418.
(45) Durham, D. B.; Ogletree, D. F.; Barnard, E. S. Scanning A uger spectromicroscopy using the S cope F oundry software platform. *Surf. Interface Anal.* **2018**, *50*, 1174−1179.
(46) Fuchs, K. In *The conductivity of thin metallic films according to the electron theory of metals*; Mathematical Proceedings of the Cambridge Philosophical Society, 1938; Cambridge University Press: 1938; pp 100−108.
(47) Sondheimer, E. H. The mean free path of electrons in metals. *Adv. Phys.* **1952**, *1*, 1−42.
(48) Majumdar, A. Microscale heat conduction in dielectric thin films. *J. Heat Transfer* **1993**, *115* (1), 7−16.
(49) Sultan, R.; Avery, A.; Underwood, J.; Mason, S.; Bassett, D.; Zink, B. Heat transport by long mean free path vibrations in amorphous silicon nitride near room temperature. *Phys. Rev. B: Condens. Matter Mater. Phys.* **2013**, *87*, 214305.
(50) Sikora, A.; Ftouni, H.; Richard, J.; Hébert, C.; Eon, D.; Omnes, F.; Bourgeois, O. Highly sensitive thermal conductivity measurements of suspended membranes (SiN and diamond) using a 3ω-Völklein method. *Rev. Sci. Instrum.* **2012**, *83*, No. 054902.
(51) Wu, X.; Hull, R. A novel nano-scale non-contact temperature measurement technique for crystalline materials. *Nanotechnology* **2012**, *23*, 465707.
(52) Wehmeyer, G.; Bustillo, K. C.; Minor, A. M.; Dames, C. Measuring temperature-dependent thermal diffuse scattering using scanning transmission electron microscopy. *Appl. Phys. Lett.* **2018**, *113*, 253101.

860 (53) Idrobo, J. C.; Lupini, A. R.; Feng, T.; Unocic, R. R.; Walden, F.
861 S.; Gardiner, D. S.; Lovejoy, T. C.; Dellby, N.; Pantelides, S. T.;
862 Krivanek, O. L. Temperature measurement by a nanoscale electron
863 probe using energy gain and loss spectroscopy. *Phys. Rev. Lett.* **2018**,
864 *120*, No. 095901.
865 (54) Lagos, M. J.; Batson, P. E. Thermometry with subnanometer
866 resolution in the electron microscope using the principle of detailed
867 balancing. *Nano Lett.* **2018**, *18*, 4556−4563.
868 (55) He, L.; Hull, R. Quantification of electron−phonon scattering
869 for determination of temperature variations at high spatial resolution
870 in the transmission electron microscope. *Nanotechnology* **2012**, *23*,
871 205705.
872 (56) Mecklenburg, M.; Hubbard, W. A.; White, E.; Dhall, R.;
873 Cronin, S. B.; Aloni, S.; Regan, B. Nanoscale temperature mapping in
874 operating microelectronic devices. *Science* **2015**, *347*, 629−632.
875 (57) Siemens, M. E.; Li, Q.; Yang, R.; Nelson, K. A.; Anderson, E.
876 H.; Murnane, M. M.; Kapteyn, H. C. Quasi-ballistic thermal transport
877 from nanoscale interfaces observed using ultrafast coherent soft X-ray
878 beams. *Nat. Mater.* **2010**, *9*, 26−30.
879 (58) Minnich, A. J.; Johnson, J. A.; Schmidt, A. J.; Esfarjani, K.;
880 Dresselhaus, M. S.; Nelson, K. A.; Chen, G. Thermal conductivity
881 spectroscopy technique to measure phonon mean free paths. *Phys.*
882 *Rev. Lett.* **2011**, *107*, No. 095901.
883 (59) Freedman, J. P.; Leach, J. H.; Preble, E. A.; Sitar, Z.; Davis, R.
884 F.; Malen, J. A. Universal phonon mean free path spectra in crystalline
885 semiconductors at high temperature. *Sci. Rep.* **2013**, *3*, 1−6.
886 (60) Li, M.; Kang, J. S.; Hu, Y. Anisotropic thermal conductivity
887 measurement using a new Asymmetric-Beam Time-Domain Ther-
888 moreflectance (AB-TDTR) method. *Rev. Sci. Instrum.* **2018**, *89*,
889 No. 084901.
890 (61) Zhang, X.; Grigoropoulos, C. P. Thermal conductivity and
891 diffusivity of free-standing silicon nitride thin films. *Rev. Sci. Instrum.*
892 **1995**, *66*, 1115−1120.
893 (62) Griffin, A., Jr; Brotzen, F.; Loos, P. The effective transverse
894 thermal conductivity of amorphous Si3N4 thin films. *J. Appl. Phys.*
895 **1994**, *76*, 4007−4011.